Nonlinear Meissner effect in a high-temperature superconductor

D. Agassi
Naval Surface Warfare Center, Carderock Division, 9500 MacArthur Boulevard, West Bethesda, Maryland 20817-5700, USA

D. E. Oates
MIT Lincoln Laboratory, 244 Wood Street, Lexington, Massachusetts 02420-9108, USA
(Received 16 July 2004; revised manuscript received 27 April 2005; published 26 July 2005)

The lowest nonlinear correction to the penetration depth, i.e., the nonlinear Meissner effect, is calculated and compared to data from high-quality $YBa_2Cu_3O_{7-\delta}$ (YBCO) films. The calculation is based on the Green-function formulation of superconductivity, and the data consist of the intermodulation power as function of temperature and circulating power. At a low power level, the calculated temperature dependence compares very well with the data, including the divergence as T^{-2} at very low temperatures. The calculated power dependence of the nonlinear penetration depth follows the data semiquantitatively and is enhanced due to the *d*-wave symmetry of the order parameter. These results support the assertion that the origin of nonlinearity in high-quality YBCO films is intrinsic. The analysis also implies that the nonlinear corrections to the penetration depth depend primarily on the total current carried by the strip and thus are insensitive to the edges. The comparison of the present approach with an alternative approach, based on quasiparticle backflow, is discussed.

DOI: 10.1103/PhysRevB.72.014538 PACS number(s): 74.25.Nf, 74.20Rp, 74.72Bk

I. INTRODUCTION

The nonlinear Meissner effect, as manifested in a current-dependent penetration depth and intermodulation distortion (IMD), was theoretically predicted for an ideal high temperature superconductor (HTS) by Yip and Sauls (YS) at $T=0$.[1] It has recently been observed over a wide range of temperatures.[2,3] While the phenomenon is experimentally well established, with important practical implications for microwave filter applications, there has been no consensus regarding its origin. Early attempts attributed it to current-driven vortex motion in weak links.[4,5] Such weak links act as Josephson junctions in which penetrating vortices obey a nonlinear dynamics, and consequently the response of the vortex-film system to a microwave field is nonlinear as well. While this mechanism is likely valid, it does not yield a quantitative explanation for high-quality films, especially at a low power level.[2] A competing view of the phenomenon is shown in the works of YS and the subsequent generalization to all temperatures.[1,6] These are based on the proposition that the observed nonlinearity is intrinsic, reflecting the highly correlated nature of the superconductor condensate state. In particular, for a superconductor with a *d*-wave symmetry order parameter (HTS), this proposition predicts a divergent nonlinear response as temperature approaches $T=0$ due to the low-lying excitations along the nodal lines. Recent attempts to compare predictions of this intrinsic mechanism with high-quality $YBa_2Cu_3O_{7-\delta}$ (YBCO) films data are encouraging.[2,7] Specifically, the predicted divergence at low temperature and the existence of two or more power regimes with different nonlinear current dependencies were observed. In this work the intrinsic nonlinear response is calculated. However, this calculation differs from the previous work[1,6] on several accounts: (1) The approach is based on the many-body formulation of superconductivity; consequently, the final expressions involve only experimentally accessible quantities. (2) The analysis implies that the nonlinear response obeys a nonlinear electrodynamics of the kind encountered in type-I superconductors. This result implies that, to a good approximation, the nonlinear corrections in films depend on the total current. (3) The theoretical analysis is compared with recent pertinent data to validate its veracity. While some of these results have been recently reported,[2] the aim here is to give a comprehensive account of our theoretical approach and extend the comparisons with the YBCO high-quality film data.

The calculation begins with the expansion of the momentum-space constitutive relation (CR) that relates the supercurrent current density $\vec{j}_S$ and the electromagnetic vector potential $\vec{A}$.[8–10] In the long wavelength limit and the cgs unit system, this CR has the form

$$\vec{j}_S = -\frac{c}{4\pi}[K_L + K_{\mathrm{NL}}(\vec{A})]\vec{A}, \tag{1.1}$$

where the chosen gauge is $\vec{\nabla}\cdot\vec{A}=0$, and K_L and $K_{\mathrm{NL}}(\vec{A})$ denote the linear and nonlinear kernels, respectively. The linear term in (1.1) is equivalent to the London theory[10] with $K_L = \lambda_0^{-2}$, where λ_0 denotes the London (linear) penetration depth. The aim here is to go beyond the linear term and calculate the lowest-order contribution in $\vec{A}$ to $K_{\mathrm{NL}}(\vec{A})$, assuming that the nonlinear corrections to the penetration depth are small.[2] It has been argued that this lowest-order contribution is of third order in $\vec{A}$.[7] Such a term, in turn, gives rise to third-order IMD products at frequencies $2f_1 - f_2$ and $2f_2 - f_1$, where the incident tones are f_1 and f_2.[2] Consequently, the IMD power generated by a film is directly related to the nonlinear quantities calculated here, and its measurement, which has the important advantage of avoiding interference from the large linear inductive

contribution,[2,11] provides a convenient test of the theory.

The paper is organized as follows. In Sec. II the microscopic approach and the derivation of the lowest order correction to the CR are presented. To render the ensuing expression tractable, a critical approximation is introduced and justified. In Sec. III this analysis yields a cubic CR in momentum space. This CR is analyzed for its implications on the nonlocality of the nonlinear current component. This analysis implies that, to a good approximation, the nonlinear correction to the penetration depth is spatially constant. In Sec. IV the solutions to the cubic CR are analyzed showing the existence of two distinct parameter regimes with different dependencies of the nonlinear penetration depth on the total current. The low-power regime is characterized by quadratic current dependence. The high-power regime is characterized by a fractional-power dependence of the absolute value of the total current, reminiscent yet different from a similar term in the YS theory.[1,6] Section V is devoted to a comparison of these theoretical results with recent IMD data from high-quality YBCO films, and Sec. VI contains a discussion of the remaining differences and a comparison with the alternative approaches to analyze nonlinearity.[1,6] Several Appendixes are included to clarify details.

II. CUBIC CONSTITUTIVE RELATION

The approach followed here is based on the Green-function formulation of superconductivity of an infinite, homogeneous sample as embodied in the imaginary-time Gorkov equations.[9]

$$\begin{pmatrix} -\frac{\hbar\partial}{\partial\tau} - \frac{1}{2m}\left(-i\hbar\vec{\nabla} - \frac{q_S}{c}\vec{A}(x)\right)^2 + \mu & \Delta(\vec{r}) \\ \Delta^*(\vec{r}) & -\frac{\hbar\partial}{\partial\tau} + \frac{1}{2m}\left(i\hbar\vec{\nabla} - \frac{q_S}{c}\vec{A}(x)\right)^2 - \mu \end{pmatrix} \begin{pmatrix} g(x,x') & f(x,x') \\ f^*(x,x') & -g(x',x) \end{pmatrix} = \hbar\delta(x-x')\overleftrightarrow{I}, \quad (2.1)$$

where $x=(\vec{r},\tau)$ denotes the four coordinates in which τ is the imaginary time in the Matsubara formalism, which is limited to $0\leqslant\tau\leqslant\beta\hbar$, $\beta=1/(k_BT)$ where k_B is the Bolztmann constant, q_S is the single-carrier charge (a positive or negative electron charge), m is the proper effective mass, μ is the chemical potential, $\overleftrightarrow{I}$ is the 2×2 unit matrix, $\Delta(\vec{r})$ is the gap function, and the ordinary and extraordinary Green functions are $g(x,x')$ and $f(x,x')$, respectively.[12] As is common in a mean field theory, the gap function and the vector potential in (2.1) must be solved self-consistently.[9] As is often the case, it will be assumed here that the gap and vector potential in (2.1) are already self-consistent quantities. This assumption is further discussed in Sec. VI.

Guided by the general structure of the CR, Eq. (1.1), the approach is to solve the Gorkov equations in perturbation theory in the vector potential.[7,9] The matrix solution of Eq. (2.1) can be formally written as an expansion in powers of the $\vec{A}$-dependent interaction

$$\hat{G} = \hat{G}_0 + \frac{1}{\hbar}\hat{G}_0\hat{W}\hat{G}_0 + \frac{1}{\hbar^2}\hat{G}_0\hat{W}\hat{G}_0\hat{W}\hat{G}_0 + \frac{1}{\hbar^3}\hat{G}_0\hat{W}\hat{G}_0\hat{W}\hat{G}_0\hat{W}\hat{G}_0 + \cdots, \quad (2.2)$$

where

$$\hat{W} = \frac{i\hbar q_S}{mc}(\vec{A}\cdot\vec{\nabla})\overleftrightarrow{I} - \frac{q_S^2\vec{A}\cdot\vec{A}}{2mc^2}\begin{pmatrix} 1 & 0 \\ 0 & -1 \end{pmatrix}. \quad (2.3)$$

In Eq. (2.2) the full Green function $\hat{G}$ and the Green function in the absence of an electromagnetic field $\hat{G}_0$ have the structure

$$\hat{G} = \begin{pmatrix} g(x,x') & f(x,x') \\ f^*(x,x') & -g(x',x) \end{pmatrix},$$

$$\hat{G}_0 = \begin{pmatrix} g_0(x,x') & f_0(x,x') \\ f_0(x,x') & -g_0(x',x) \end{pmatrix}, \quad (2.4)$$

where the entries in $\hat{G}_0$ are given in Appendix A. In terms of the Green function (2.4), the CR that connects the current density and vector potential is consequently obtained from the general relation[9]

$$\vec{j}(x) = 2\left\{\frac{i\hbar q_S}{2m}(\vec{\nabla}_{\vec{r}'} - \vec{\nabla}_{\vec{r}})g(x,x') - \frac{q_S^2}{mc}\vec{A}(x)g(x,x')\right\}_{\substack{\vec{r}'\to\vec{r} \\ \tau'\to\tau+0^+}}. \quad (2.5)$$

The last term in Eq. (2.5) contributes only to the linear term in the CR noting that $g(x,x)$ is expressible in terms of the total number of carriers n_{TOT}. Thus, all nonlinear terms in the CR arise from the first term in Eq. (2.5). While this scheme for deriving the nonlinear CR appears straightforward, simplifying assumptions are critical to render it tractable. These assumptions, to which we turn now, should be considered as part of our approach.

As a first simplifying approximation, we consider only the static limit, i.e., when $\vec{A}(\vec{r},t)\approx\vec{A}(\vec{r})$. As empirically demonstrated,[3] this is an excellent approximation, consistent with the argument that the characteristic energy scales at microwave frequencies obey $\hbar\omega\ll|\Delta|$. Next, the interaction $\hat{W}$, Eq. (2.2), is simplified. Noting that the structure of Eq. (2.3) is $\hat{W}=\alpha_1(\vec{A}\cdot\vec{\nabla})+\alpha_2(\vec{A}\cdot\vec{A})$, the relative importance of

these two terms is estimated in two ways. In the first way, note from Eqs. (2.2) and (2.3) that there are two third-order terms in the expansion. Their ratio is roughly

$$\frac{\hat{G}_0^4\alpha_1^3(\vec{A}\cdot\vec{\nabla})^3v^3}{\hbar\hat{G}_0^3\alpha_1(\vec{A}\cdot\vec{\nabla})\alpha_2(\vec{A}\cdot\vec{A})v^2}\sim\frac{\alpha_1^2\hat{G}_0v}{\hbar\alpha_2\ell^2}, \tag{2.6}$$

where v denotes a characteristic intermediate-integration volume (in real space and in the τ variable) and ℓ is a characteristic length associated with the gradient action on an unperturbed Green function. Denoting by ξ the coherence length, adopting the order-of-magnitude estimates $\hat{G}_0\sim\xi^{-3}$, $v\sim\xi^3(\hbar/\Delta)$,[9] and inserting the expressions for $\{\alpha_1,\alpha_2\}$ from Eq. (2.3) and the coherence length estimate $\xi\sim\hbar^2k_F/m\Delta$,[10] it follows that the ratio in Eq. (2.6) is $\approx O(1)$.

The second approach to estimate the ratio of the two terms in $\hat{W}$ is to take the London expression for the vector potential $A=4\pi j_S\lambda^2/c$, $\nabla\sim\xi^{-1}$, and $j_S\sim j_{\mathrm{DEPAIR}}\sim10^8$ A/cm^2, where j_{DEPAIR} is the depairing current for YBCO. This estimate yields again that the two terms in the interaction $\hat{W}$ are of about equal importance. Either way, since factors of $O(1)$ are beyond the accuracy scope of the present calculation, we conclude that for our purpose, it is justified to approximate

$$\hat{\mathrm{W}}\approx\frac{i\hbar q_S}{mc}(\vec{A}\cdot\vec{\nabla})\vec{\vec{I}}. \tag{2.7}$$

The basic expression for the third-order correction to the CR is then obtained by combining Eqs. (2.2), (2.5), and (2.7),[7]

$$\begin{aligned}\vec{j}_S^{\,(3)}(\vec{r})&=2\left\{\frac{i\hbar q_S}{2m}(\vec{\nabla}_{\vec{r}\prime}-\vec{\nabla}_{\vec{r}})g^{(3)}(x,x')\right\}_{\substack{\vec{r}\prime\to\vec{r}\\ \tau'\to\tau+0^+}}\\&=-2\frac{i\hbar q_S}{m}\frac{1}{\hbar^3}\left(\frac{i\hbar q_S}{mc}\right)^3\vec{\nabla}_{\vec{r}}\{\langle x|\hat{G}_0(\vec{A}\cdot\vec{\nabla})\vec{\vec{I}}\hat{G}_0(\vec{A}\cdot\vec{\nabla})\\&\quad\times\vec{\vec{I}}\hat{G}_0(\vec{A}\cdot\vec{\nabla})\vec{\vec{I}}\hat{G}_0|x'\rangle_{(1,1)}\}_{\substack{\vec{r}\prime\to\vec{r}\\ \tau'\to\tau+0^+}}.\end{aligned} \tag{2.8}$$

A significant simplification of Eq. (2.8) is obtained by considering the one-dimensional geometry shown in Fig. 1, where $w\gg d\sim\lambda$ and the magnetic field wraps around the strip. In this case the Meissner effect is realized primarily in the y direction, the current density peaks at the strip edges, and is to a good approximation uniform in the z direction. Therefore, we have[13]

$$\vec{j}(\vec{r})=(j_x(y),0,0),\quad \vec{A}(\vec{r})=(A_x(y),0,0),$$

$$\vec{H}(\vec{r})=(0,0,H_z(y)),\quad \vec{\nabla}\cdot\vec{A}=0. \tag{2.9}$$

The coordinate-system choice in Fig. 1, however, does not conform to standard notations where, for a finite (or infinite) thickness slab, the Meissner effect is realized in the z coordinate aligned normal to its surface. Therefore, while the expressions below employ the standard z axis as the coordinate in which the Meissner effect is realized, the pertinent

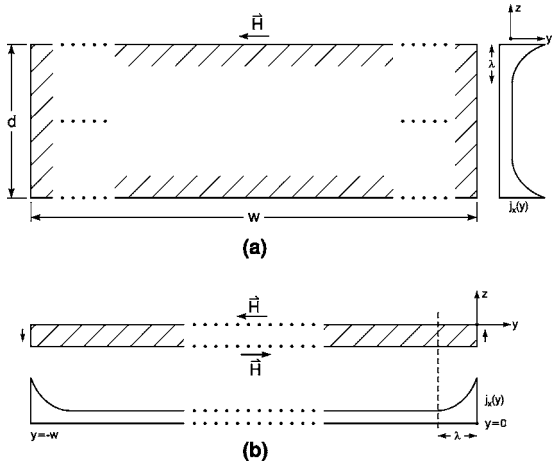

FIG. 1. Key parameters, coordinate system, and schematic current distribution of a superconductor strip. (a) A thick strip ($w\gg d\gg\lambda$) cross section. (b) A thin strip in a stripline resonator ($w\gg d\sim\lambda$).

film dimension is w in keeping with the configuration in Fig. 1.

Inserting the unperturbed Green's functions given in Appendix A into Eq. (2.8), taking the one-dimensional Fourier transform, performing all spatial and temporal intermediate integrations and summations (see Appendix A), and employing the vector-potential transversality, $\vec{k}\cdot\vec{A}(\vec{k})=0$, (Eq. (2.9)) yields

$$\begin{aligned}\vec{j}^{(3)}(q)&=\int_{-\infty}^{\infty}dze^{-iqz}\vec{j}^{(3)}(z)\\&=\frac{2{q_S}^4}{\beta(2\pi)^5m^4c^3}\sum_{n=-\infty}^{\infty}\int d\vec{k}_1dq_1dq_2\vec{k}_1\{\hat{G}_0(\vec{k}_1,\omega_n)\\&\quad\times[\vec{A}(\vec{q}_1)\cdot\vec{k}_1]\vec{\vec{I}}\hat{G}_0(\vec{k}_1-\vec{q}_1,\omega_n)[\vec{A}(\vec{q}_2)\cdot\vec{k}_1-\vec{q}_1]\vec{\vec{I}}\hat{G}_0(\vec{k}_1\\&\quad-\vec{q}_1-\vec{q}_2,\omega_n)[\vec{A}(\vec{q}-\vec{q}_1-\vec{q}_2)\cdot\vec{k}_1-\vec{q}]\vec{\vec{I}}\hat{G}_0(\vec{k}_1\\&\quad-\vec{q},\omega_n)\}_{(1,1)},\end{aligned} \tag{2.10}$$

where the Matsubara frequencies ω_n are given in (A.2). The complex structure of the expression in Eq. (2.10) can be inferred directly from the diagram in Fig. 2, noting that momentum is conserved at each vortex. Recall also that it is assumed that both the gap function and in particular the vector potential, e.g., in Eq. (2.10), are self-consistent. For the latter, this implies a functional dependence on the sample

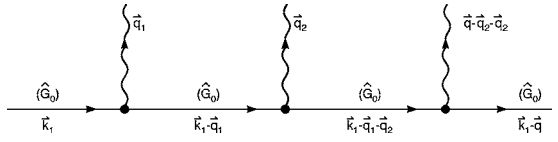

FIG. 2. Diagram representing the third-order term in the current density perturbative expansion, Eq. (2.10). Each bullet represents the momentum-conserving vector-potential interaction Eq. (A.5) for the one-dimensional geometry of this work.

edge coordinate z_0, e.g., $\vec{A}(\vec{r}) \approx \vec{A}(z-z_0)$, to provide a reference point where the magnetic-field attenuation starts.[14] This observation is important for the following developments.

The fivefold integration in Eq. (2.10) can be reduced to a one-dimensional integration by invoking an approximation based on decoupling the integrations, an integrand expansion around its maximum in the $\{q_1, q_2\}$ space, and the standard retention of contributions only from the immediate proximity of the Fermi surface; see Appendixes B and C. Due to its particular importance, this reduction in the number of integrations is detailed next.

Note first that the homogeneous Green function $\hat{G}_0(\vec{k}, \omega_n)$ draws its main contribution from momenta near the Fermi surface $|\vec{k}| \sim k_F$,[9] while the self-consistent $\vec{A}(\vec{q})$, approximately a Lorentzian, is significant only for $0 < q \leqslant 1/\lambda \ll k_F$. Consequently, in all Green-function factors in Eq. (2.10), the q_1 and q_2 dependencies can be neglected and the $\{q_1, q_2\}$ integrations are constrained only by the scalar-product factors which are discussed now. Denoting by $\vec{A} \| \vec{B}$ parallel vectors $\vec{A}$ and $\vec{B}$, the integrand in Eq. (2.10) attains maximum in the (q_1, q_2) space at the point where

$$\vec{A}(\vec{q}_2) \| \vec{k}_1 - \vec{q}_1, \tag{2.11a}$$

$$\vec{A}(\vec{q} - \vec{q}_1 - \vec{q}_2) \| \vec{k}_1 - \vec{q}, \tag{2.11b}$$

$$\vec{A}(\vec{q}_1) \| \vec{k}_1. \tag{2.11c}$$

Consider first conditions (2.11a) and (2.11b). Both are simultaneously satisfied provided $\vec{q} = \vec{q}_1$ since for a real one-dimensional vector potential $\vec{A}(\vec{q}) = \vec{A}^*(-\vec{q})$. Furthermore, noting that the $\vec{k}_1$ integration draws its main contribution when $|\vec{k}_1| \sim k_F \gg |q_1|, |q_2|$,[9] it follows that all maximum-overlap conditions in Eq. (2.12) are approximately satisfied at the point $\vec{q}_1 = \pm \vec{q}_2 = \vec{q}$. This outcome suggests an integrand expansion in terms of new variables $\vec{q}_1 = \vec{q} + \vec{\kappa}_1$, $\vec{q}_2 = -\vec{q} + \vec{\kappa}_2$, where the integrand is expected to fall off significantly over the range $|\vec{\kappa}_1, \vec{\kappa}_2| \leqslant 1/\lambda$. While the details of this falloff are complicated, it is presumed that only the maximum value and falloff range of the integrand impact significantly the magnitude of the integral.

To quantify this assertion, two plausible analytic forms are explored, both of which share the same maximum value and falloff range λ_0 yet differ in the rate of the falloff. Specifically, consider

$$\mathbb{R}(\kappa) = \frac{\vec{A}(q+\kappa) \cdot \vec{k}_1}{\vec{A}(q) \cdot \vec{k}_1} = \begin{cases} e^{-(\kappa^* \lambda_0)^2} \\ 1/[1 + (\kappa^* \lambda_0)^2]. \end{cases} \tag{2.12}$$

The corresponding q_1 and q_2 integrations in Eq. (2.10) are analytically available, namely,

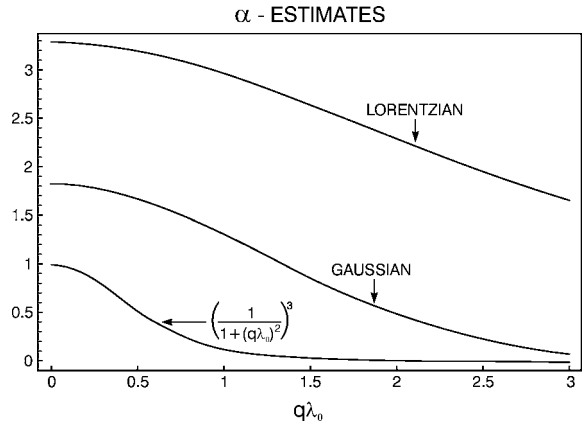

FIG. 3. The function $F(q\lambda)$ defined in Eq. (2.13) for the assumed Lorentzian and Gaussian form factors, see text. The $[1 + (q\lambda_0)^2]^{-3}$ curve is added for the purpose of delineating the pertaining range of the variable $q\lambda_0$.

$$\int_{-\infty}^{\infty} d\kappa_1 \int_{-\infty}^{\infty} d\kappa_2 \mathbb{R}(\kappa_1)\mathbb{R}(\kappa_1)\mathbb{R}(q - \kappa_1 - \kappa_2)$$
$$= \frac{1}{\lambda_0^2} \begin{cases} \pi e^{-(q\lambda_0)^2}/\sqrt{3} \\ \dfrac{3\pi^2}{9 + (q\lambda_0)^2} \end{cases} = \frac{F(q\lambda_0)}{{\lambda_0}^2}. \tag{2.13}$$

As Fig. 3 shows, the approximation $F(x) \approx \alpha = 2-3$ holds over the pertinent range of $q\lambda \leqslant O(1)$. Consequently, the $\{q_1, q_2\}$ integrations in (2.10) are approximated by

$$\int dq_1 dq_2 [\vec{A}(\vec{q}_1) \cdot \vec{k}_1][\vec{A}(\vec{q}_2) \cdot \vec{k}_1 - \vec{q}_1][\vec{A}(\vec{q} - \vec{q}_1 - \vec{q}_2) \cdot \vec{k}_1 - \vec{q}_1]$$
$$\approx \frac{\alpha}{{\lambda_0}^2} [\vec{A}(\vec{q}) \cdot \vec{k}_1]^2 [\vec{A}(-\vec{q}) \cdot \vec{k}_1], \tag{2.14}$$

where $\alpha = O(2-3)$ is a dimensionless constant. Applying these approximations to Eq. (2.10) yields the expression for the third-order correction to the Cooper-pairs current

$$\vec{j}_S^{(3)}(q) = -\frac{2{q_q}^4 \alpha}{\beta(2\pi)^5 m^4 c^3 \lambda_0^2} \sum_{n=-\infty}^{\infty} \int d\vec{k}_1 \vec{k}_1 [\vec{A}(\vec{q}) \cdot \vec{k}_1]^2$$
$$\times [\vec{A}(-\vec{q}) \cdot \vec{k}_1] \{[\hat{G}_0(\vec{k}_1, \omega_n)]^4\}_{(1,1)}. \tag{2.15}$$

The steps leading to Eq. (2.15) are based only on general properties of the vector potential, the unperturbed Green's function, and the Fermi surface. The remaining integrations in Eq. (2.15) depend on details such as the gap-function symmetry and Fermi-surface shape. In particular, it is of interest to compare Eq. (2.15) for the case of a gap function with an s-wave symmetry and a cylindrical Fermi surface to a previous calculation elsewhere employing a different method.[7] In Appendix B it is shown that they are equivalent.

In HTS, on the other hand, the gap function has $d_{x^2-y^2}$-wave symmetry and an approximately cylindrical Fermi surface.[16] The details of the angular integrations in Eq.

(2.15) are given in Appendix C. Combining all these steps together yields the momentum-space (lowest-order) nonlinear CR for *d*-wave superconductors,

$$\vec{j}_S(q) = -\frac{c}{4\pi}\left(\frac{1}{\lambda_0^2(T)} + K^{(2)}(T)|A(q)|^2\right)\vec{A}(q), \quad (2.16)$$

where

$$K^{(2)}(T) = \frac{{q_S}^4 \alpha \mu^2 k_F(\hat{c})}{\pi^3 \beta m_{ab} c^2 (\hbar c)^2 [\lambda_0(T)]^2 [\Delta_0(T)]^3} \times \sum_{n=-\infty}^{\infty} \int_0^{2\pi} d\theta (\cos^4\theta) \times (\cos^2 2\theta) \frac{\cos^2 2\theta - [2\hbar\omega_n/\Delta_0(T)]^2}{\{\cos^2 2\theta + [\hbar\omega_n/\Delta_0(T)]^2\}^{7/2}}. \quad (2.17)$$

Expressions (2.16) and (2.17) are the central results of this work. The symbols $k_F(\hat{c})$ and m_{ab} denote the Fermi momentum in the $\hat{c}$ direction ($\approx \pi/a_c$, where a_c is the lattice constant in the c direction) and the effective mass in the ab plane, respectively, and the gap $\Delta_0(T)$ is defined in Appendix A. Note that Eqs. (2.16) and (2.17) contain only measurable quantities with the exception of the dimensionless α factor, which is, however, bracketed within a narrow range. Consequently, a comparison of Eq. (2.16) with data provides a stringent test to this result.

The angular integral in Eq. (2.17) can be further expressed in closed form; see Appendix D. Note that conforming to the assumed one-dimensional geometry (Fig. 1) and the Fourier transform defined in Eq. (A.5), the vector current density and vector potential are related to the corresponding scalar quantities by

$$\vec{j}(q) = \hat{x} j(q), \quad \vec{A}(q) = \hat{x} A(q). \quad (2.18)$$

III. NONLINEARITY AND NONLOCALITY

To introduce the issue of nonlocality in nonlinearity, consider the general connection between the momentum-space CR and its real-space counterpart,[16]

$$\vec{j}(q) = -\frac{c}{4\pi} K(q)\vec{A}(q) \Leftrightarrow \vec{j}(\vec{r}) = C\int \frac{\vec{R}[\vec{R}\cdot\vec{A}(\vec{r}')]}{R^4} K(R) d\vec{r}', \quad \vec{R} = \vec{r} - \vec{r}', \quad (3.1)$$

where the current densities in momentum and real spaces are $\vec{j}(\vec{q})$ and $\vec{j}(\vec{r})$, respectively, and the S subscript attached to the current densities is omitted to simplify the notation, the symbol $\Leftrightarrow$ indicates that both expressions are related by a linear transform of each other,[16] C is an unimportant normalization constant, and the kernels $K(\vec{q})$ and $K(R)$ are related to each other via a linear Bessel transform, which implies that their ranges in momentum and real spaces, respectively, are inversely proportional to each other.[16]

The linear approximation for $K(\vec{q})$ corresponds to $K(R) \sim e^{-R/\xi}$ (Ref. 16) since the linear term in $\hat{W}$ in Eq. (2.2) involves only the unperturbed Green functions, which attenuates over the length scale of ξ. The self-consistent vector potential, on the other hand, attenuates over a distance λ_0 from the sample edge. Consequently, Eq. (3.1) implies that when $\lambda_0 \gg \xi$, the fastest varying factor in the integrand is $K(R)$; hence it is justified to pull $\vec{A}(\vec{r}') \approx \vec{A}(\vec{r})$ from under the integral. This yields a linear and local CR, which is a restatement of the London theory for type II superconductors. In the opposite limit, however, when $\lambda_0 \ll \xi$, the variation of $K(R)$ in the integrand of Eq. (3.1) is slow in comparison to that of the other factors, resulting in a nonlocal CR, characteristic of the Pippard theory of type I superconductors.[17]

These considerations are now applied to the nonlinear term in Eq. (2.16), which is the focus of this work. Since the transformation connecting $K(q)$ and $K(R)$ in (3.1) is linear, it follows, with self-evident notation, that

$$K(q) = K^{(0)} + K^{(2)}(T)|A(q)|^2 \Leftrightarrow K(R) = K^{(0)}(R) + K^{(2)}(R) \Rightarrow \vec{j}(\vec{r}) = \vec{j}_L(\vec{r}) + \vec{j}_{\mathrm{NL}}(\vec{r}), \quad (3.2)$$

where we employed Eq. (2.16) and wrote $K^{(2)}(q) = K^{(2)}(T) \times |A(q)|^2$ and the current densities $\vec{j}_L$ and $\vec{j}_{\mathrm{NL}}$ denote the linear and nonlinear current densities associated with the corresponding terms in $K(q)$. The $|A(q)|^2$ factor in the nonlinear kernel in Eq. (2.16) implies a momentum-space range that is roughly half that of $A(q)$, i.e., $(2\lambda_0)^{-1}$. Hence the range L of its real-space counterpart $K^{(2)}(R)$ is $L \sim 2\lambda_0$. According to relation (3.1), $K^{(2)}(R)$ with this range implies a $\vec{j}_{\mathrm{NL}}$ in Eq. (3.2) that is related to the vector potential through a nonlocal CR. The particular nonlocal, linear CR encountered in type I superconductors represents the case when the range of $K(R)$, i.e., ξ, is considerably smaller than the range of $\vec{A}(\vec{r})$, i.e., λ_0.[17] This qualitative argument implies that all higher nonlinear terms in Eq. (2.2) would also lead to a nonlocal CR. Because of their small magnitude these nonlocal contributions can be ignored in most cases so that the London theory applies.

The same qualitative conclusion follows from consideration of the structure of the real-space expression for the nonlinear current density $\vec{j}_{\mathrm{NL}}(z)$, Eq. (2.8). Consider a typical term in that expression

$$\int dz_1 dz_2 dz_3 g_0(z - z_1) A(z_1 - z_E) g_0(z_1 - z_2) A(z_2 - z_E) g_0(z_2 - z_3) A(z_3 - z_E) g_0(z_3 - z). \quad (3.3)$$

The vector-potential dependence on the edge location z_E, e.g., through a cusplike functional form,[14] is explicitly retained in (3.3). The homogeneous Green function factors $g_0(z')$ are negligible for $|z'| > \xi$, while the vector-potential factors are negligible for $|z' - z_E| \geqslant \lambda_0$. Since in HTS $\lambda_0 \gg \xi$, it follows that the z coordinate in Eq. (3.3) is approximately constrained by $|z - z_E| \leqslant \lambda_0$. Therefore $\vec{j}_{\mathrm{NL}}(z)$ and $A(z - z_E)$ are

related in (3.1) by a nonlocal kernel of range $O(\lambda_0)$.

The real-space nonlocality implied by the nonlinear CR of Eq. (2.16) has important implications for the methodology of data analysis and the relative importance of the strip edges. Consider the linear and perturbed current densities in Eq. (3.2), expressed in terms of the linear (London) superfluid velocity $v_S^{(0)}(\vec{r};\lambda_0)$ and linear and perturbed pair densities $n_S^{(0)}(\vec{r}), n_S(\vec{r})$,

$$\vec{j}(\vec{r}) = n_S(\vec{r}) q_{2S} \vec{v}_S^{(0)}(\vec{r};\lambda_0), \quad \vec{j}_L(\vec{r}) = n_S{}^{(0)} q_{2S} \vec{v}_S^{(0)}(\vec{r};\lambda_0), \tag{3.4}$$

where q_{2S} denotes the Cooper-pair charge. The temperature is assumed to be sufficiently low to assure a preponderance of pair current. To calculate the perturbed pair density in Eq. (3.4), insert Eq. (2.16) into Eq. (3.1) with the result

$$\vec{j}_{\mathrm{NL}}(\vec{r}) = C \int \frac{\vec{R}[\vec{R}\cdot A(\vec{r}')]}{R^4} K^{(2)}(R;r_E) d\vec{r}',$$

$$\sim C\gamma^{(2)} \int \frac{\vec{R}[\vec{R}\cdot \vec{A}(\vec{r}')]}{R^4} e^{-R/(2\lambda_0)} d\vec{r}'$$

$$\approx n_S^{(2)} q_{2S} \vec{v}_S^{(0)}(\vec{r};2\lambda_0). \tag{3.5}$$

In going from the first to the second line in Eq. (3.5), two arguments were invoked. First, as argued above, the approximate range L of the kernel $K^{(2)}(R)$ is $L \sim 2\lambda_0$. Therefore, the integration in the second integral in (3.5) has the effect of spatially averaging the factor $\vec{A}(\vec{r}) \propto \vec{v}_S^{(0)}(\vec{r};\lambda_0)$ (since in the London theory $\vec{j}_L \propto \vec{A}$) over a sliding window of extension $2\lambda_0$. The ensuing smeared-out superfluid velocity therefore has the approximate functional dependence $\vec{v}^{(0)}(\vec{r};2\lambda_0)$ and small amplitude $n_S^{(2)}$. Inserting Eq. (3.5) into Eqs. (3.4) and (3.2) yields for the total pair density the approximate expression

$$n_S(\vec{r}) = n_S^{(0)} + n_S^{(2)} \frac{\vec{v}_S^{(0)}(\vec{r};2\lambda_0)}{\vec{v}_S^{(0)}(\vec{r};\lambda_0)} = n_S^{(0)} + n_S^{(2)}(\vec{r}). \tag{3.6}$$

The structure of expression (3.6) implies a weak spatial dependence for the nonlinear superfluid density $n_S^{(2)}(\vec{r})$ since it entails a ratio of two superfluid velocities where their corresponding peaks at the strip edges cancel out. This point is demonstrated in Fig. 4 where we plot the ratio $\vec{v}_S^{(0)}(\vec{r};2\lambda_0)/\vec{v}_S^{(0)}(\vec{r};\lambda_0)$ in Eq. (3.6) for a typical current distribution in a thin film.[23] Therefore the total pair density $n_S(\vec{r})$ is essentially constant throughout the strip width except for a mild dip (factor 2) at the strip edges which can be ignored.

The conclusion of an approximately constant superfluid density depends only on the CR structure, not on particulars of functional dependencies. It implies considerable simplification of the functional relation between the momentum-space CR, Eq. (2.16), by providing justification for considering only the long-wavelength limit $q=0$ of the CR. Consequences of this conclusion are taken up in the following sections.

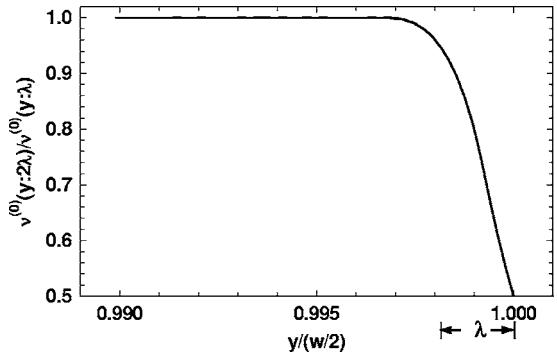

FIG. 4. The near-edge ratio $v_S(y;2\lambda_0)/v_S(y;\lambda_0)$, Eq. (3.6), for the approximate thin-film superfluid velocity distribution of Ref. 23. The parameters employed are $w=150\ \mu$m, $\lambda=150$ nm, $d=0.35$ nm, which correspond to the actual stripline resonator. Except at the very edge where this ratio is 0.5, this ratio is unity.

IV. THE PENTRATION DEPTH

Having justified the approximation that the nonlinear superfluid density is constant throughout the strip width, we extract the penetration depth from the CR long-wavelength limit by following the classic Meissner-effect paradigm.[9,10] Thus

$$\frac{1}{\lambda^2} \equiv K(q=0;T) = \frac{1}{(\lambda_0+\lambda_{\mathrm{NL}})^2}$$

$$= \frac{1}{\lambda_0{}^2} - \frac{2\lambda_{\mathrm{NL}}}{\lambda_0{}^3} + \cdots = \frac{1}{\lambda_0{}^2} + K^{(2)}(T)|A(q=0)|^2. \tag{4.1}$$

The nonlinear corrections to the penetration depth are very small. Consequently,

$$\lambda_{\mathrm{NL}} = -\frac{\lambda_0{}^3}{2} K^{(2)}(T)|A(q=0)|^2$$

$$= \frac{\lambda_0 p}{2}|A(q=0)|^2,$$

$$p = p(T) = -\lambda_0{}^2(T) K^{(2)}(T) > 0. \tag{4.2}$$

The positive parameter p introduced in (4.2) is useful for the manipulations below.

In principle, the nonlinear penetration depth in Eq. (4.2) is the end result of the analysis. However, to allow comparison with data it is necessary to express the vector potential factor $A(q=0)$ in it in terms of measurable quantities, e.g., the current. This requires the inversion of the long-wavelength-limit cubic CR [Eq. (2.17)]

$$j(q=0) = -\frac{c}{4\pi\lambda_0{}^2}[1-p|A(q=0)|^2]A(q=0), \tag{4.3}$$

where the $j(q=0)$ factor according to the discussion in Sec. II and Eq. (A.5) is given by

$$j(q=0)=\int_{-w}^{0} dz j_x(z)=w\langle j_x(z)\rangle_z=\frac{I}{d}. \tag{4.4}$$

In Eq. (4.4) I is the total current carried by the strip and d is its thickness, Fig. 1.

Given the expression for the nonlinear penetration depth Eq. (4.2), it is suggestive to recast Eq. (4.3) by multiplying it by its complex conjugate

$$|\vec{j}(q=0)|^2=\left(\frac{c}{4\pi\lambda_0{}^2}\right)^2(1-pS)^2S, \quad S=|\vec{A}(q=0)|^2>0. \tag{4.5}$$

The exact solutions of (4.5) are given by

$$\{S_{(1)},S_{(2)},S_{(3)}\}=-\frac{1}{3p\rho}\{(-1+\rho)^2,$$

$$[(-1)^{1/3}+(-1)^{2/3}\rho]^2,$$

$$[(-1)^{2/3}+(-1)^{1/3}\rho]^2, \tag{4.6}$$

where

$$\rho=[1-2\varepsilon+\sqrt{\varepsilon(-1+\varepsilon)}]^{1/3},$$

$$(-1)^{1/3}=\frac{(1+i\sqrt{3})}{2}, \quad (-1)^{2/3}=\frac{(-1+i\sqrt{3})}{2}, \tag{4.7}$$

and the dimensionless, positive control parameter

$$\varepsilon=\varepsilon(I,T)$$
$$=\frac{108\pi^2\lambda_0{}^6(T)|j(q=0)|^2|K^{(2)}(T)|}{c^2}=\frac{108\pi^2\lambda_0{}^6(T)I^2|K^{(2)}(T)|}{c^2d^2} \tag{4.8}$$

carries the nontrivial dependencies on both the total current and temperature. Note that ε scales with the circulating power [see Eq. (5.7)] and has a nontrivial temperature dependence.

Of the three mathematical solutions in Eq. (4.6), only one has physical meaning. To identify the physical solution, consider two limits. When $\varepsilon\ll 1$, which corresponds to the low-circulating-power limit, Eq. (4.6) is

$$\lim_{\varepsilon\ll 1}\{S_{(1)},S_{(2)},S_{(3)}\}=\frac{1}{p}\left\{\frac{4\varepsilon}{27}+O(\varepsilon^2),1+\frac{2\sqrt{\varepsilon}}{3\sqrt{3}}+O(\varepsilon^{3/2}),\right.$$
$$\left.1-\frac{2\sqrt{\varepsilon}}{3\sqrt{3}}+O(\varepsilon^{3/2})\right\}. \tag{4.9}$$

While all solutions in Eq. (4.9) are real and positive, the last two do not vanish in the limit of a vanishing small ε and hence are inconsistent with the linear London theory Eq. (1.1) at that limit. Thus, for $\varepsilon\ll 1$, the $S_{(1)}$ solution in Eq. (4.6) is the physical solution. From Eq. (4.5), the expression for $S_{(1)}$ in Eq. (4.9) and Eq. (4.8) yields

$$\lim_{\varepsilon\ll 1}|A(q)|^2=\frac{16\pi^2|j(q=0)|^2\lambda_0{}^4}{c^2}\propto I^2, \tag{4.10}$$

precisely the square of the linear London theory CR [see Eq. (1.1)].[10] This corresponds to the limit when the cubic term in the nonlinear CR can be neglected.

The opposite limit, $\varepsilon\gg 1$, corresponds to a high circulating power. Expanding (4.6) to lowest order in ε^{-1} yields

$$\lim_{\varepsilon\gg 1}\{S_{(1)},S_{(2)},S_{(3)}\}=\frac{2^{2/3}\varepsilon^{1/3}}{3p}\left\{\frac{i}{2}(i+\sqrt{3})+\frac{2^{1/3}}{\varepsilon^{1/3}},1+\frac{2^{1/3}}{\varepsilon^{1/3}},\right.$$
$$\left.-\frac{i}{2}(-i+\sqrt{3})+\frac{2^{1/3}}{\varepsilon^{1/3}}\right\}+O(\varepsilon^{-1/3}). \tag{4.11}$$

The physical solution in this limit is readily identified as $S_{(2)}$ since it is the only real one. Employing again Eqs. (4.8) and (4.11) for $S_{(2)}$ yields

$$\lim_{\varepsilon\gg 1}|A(q=0)|^2=\frac{2^{4/3}\pi^{2/3}\lambda_0{}^{4/3}|j(q=0)|^{2/3}}{(cp)^{2/3}}\propto|I|^{2/3}, \tag{4.12}$$

which is the solution of Eq. (4.5) in the limit when the cubic term dominates. Note that the dependence on a fractional power of the current in Eq. (4.11) is nonanalytic and different from that in the low-power regime, Eq. (4.10). This nonanalyticity is reminiscent but distinct from the work of Yip and Sauls[1] and Dahm and Scalapino.[6]

Given that the physical solutions yield different current dependencies in the limits $\varepsilon\gg 1$ and $\varepsilon\ll 1$, it is of particular interest to explore the nature of the transition between them. Figure 5 shows an example of the exact solutions, Eq. (4.6), plotted over the entire range of ε range to provide insight. The special role of the $\varepsilon=1$ point in Fig. 5 is obvious from the explicit form Eq. (4.7). In particular, expanding the physical solutions $S_{(1)}$ and $S_{(2)}$ around the appropriate sides of the $\varepsilon=1$ point yields

$$\lim_{\varepsilon\to 1+0}S_{(2)}-\lim_{\varepsilon\to 1-0}S_{(1)}=\frac{3}{p}, \tag{4.13}$$

indicating a discontinuity. As discussed in the next section, measured data shows no discontinuity, suggesting that the discontinuity Eq. (4.13) is a mathematical artifact, probably related to the truncation of the perturbation expansion, Eq. (2.2), at the third order. It is therefore inferred that the physical solutions in (4.6) are not reliable too close to the discontinuity point. Note that on both sides of the discontinuity, the delineation between the low- and high-power regimes as determined by the ε parameter depends on both temperature and total current. This qualitative feature is supported by the data.[2,18]

In summary, since $\lambda_{NL}\propto|A(q)|^2$, Eq. (4.2), the CR approach of this work predicts a current dependence $\lambda_{NL}\sim I^2$ in the low-power regime ($\varepsilon\ll 1$) and $\lambda_{NL}\sim|I|^{2/3}$ in the high-power regime ($\varepsilon\gg 1$).

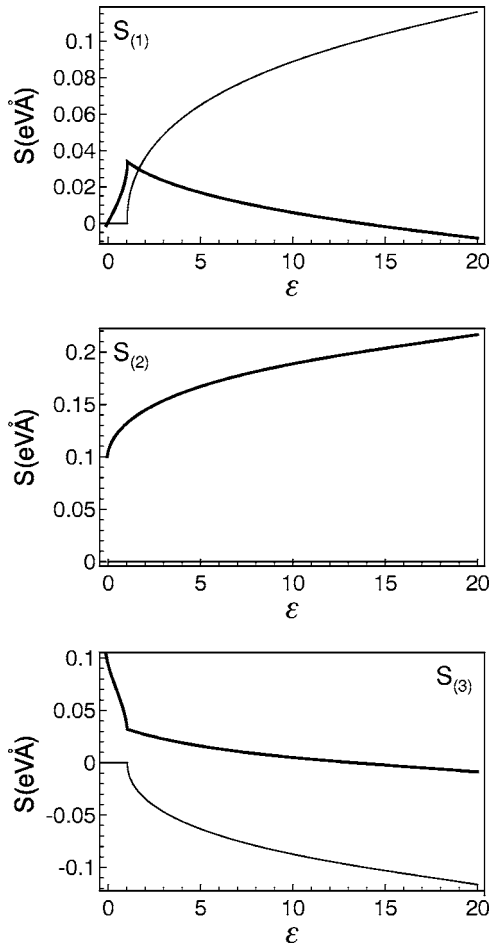

FIG. 5. The constitutive-relation solutions for the case $p = 10$ eV × Å, Eq. (4.6). The real and imaginary parts are denoted by the thick and thin lines, respectively. The three CR solutions demonstrate the special role of the $\varepsilon = 1$ point as expressed in Eq. (4.7).

V. COMPARISON WITH EXPERIMENT

In this section the preceding calculated results are compared with measurements of IMD power and surface impedance in a stripline resonator as reported elsewhere.[2,11] In the IMD measurements, the resonator is excited by two closely spaced tones at frequencies f_1 and f_2, and the IMD power is measured at $2f_1 - f_2$ and $2f_2 - f_1$.[11] This method is of high sensitivity. To measure the nonlinear surface impedance, the resonance frequency and Q are measured as a function of the total current in the strip I. The frequency shift Δf reflects the current-induced variation of the kinetic inductance, which is related to the nonlinear correction to the penetration depth λ_{NL}.[6] Measurement of Δf, however, is limited to medium currents, on the order of $I = 100$ mA, while IMD measurements can be carried out with currents of the order $I = 1$ mA.

Consider first the IMD measurement method. For a purely harmonic incident field at frequency ω, the two-fluid-model, cycle-averaged, surface electromotive force is[12,19]

$$V_S = iX_S I = i\frac{4\pi\omega}{c^2}\lambda I = i\frac{4\pi\omega}{c^2} I[\lambda_0 + \lambda_{\mathrm{NL}}(I,T)], \quad (5.1)$$

where the nonlinear part of the surface electromotive force is

$$V_S^{(\mathrm{NL})} = i\frac{4\pi\omega}{c^2} I\lambda_{\mathrm{NL}}(I,T). \quad (5.2)$$

We have neglected the contribution to $V_S^{(\mathrm{NL})}$ from the nonlinear resistance. Dahm and Scalapino have argued that it is small,[6] and experimentally, the nonlinear reactance $X_S^{(\mathrm{NL})} \times (I,T)$ and nonlinear resistance $R_S^{(\mathrm{NL})}(I,T)$ are proportional over wide ranges of current and temperature.[2,3] Thus a nonlinear resistance would at most contribute a correction with the same temperature and current dependence as the nonlinear reactance. The power delivered to the measurement system is proportional to the square of $V_S^{(\mathrm{NL})}$

$$P_{\mathrm{NL}} \propto (V_S^{(\mathrm{NL})})^2 \propto [I\lambda_{\mathrm{NL}}(I,T)]^2. \quad (5.3)$$

Expression (5.3) is now extended to the case of two tones by invoking our underlying assumption that the nonlinear penetration depth is approximately frequency independent and the measured IMD power is equated with the nonlinear power component $P_{\mathrm{IMD}} = P_{\mathrm{IMD}}(I,T) \propto P_{\mathrm{NL}}$, where we assume that the IMD power delivered to the measurement system is proportional to the IMD power circulating in the resonator. We have ignored the power at other mixing frequencies and at the third harmonic because the other components are not resonant, as are the IMD components. Consequently, from Eqs. (4.2), (4.5), and (4.6), we have

$$P_{\mathrm{IMD}} = C(T) I^2 S_P^2[\varepsilon(I,T)], \quad S(\varepsilon) = \frac{S_p}{3p}, \quad (5.4)$$

where all purely temperature-dependent prefactors, such as $p(T)$ and $\lambda_0(T)$, are lumped into $C(T)$, and S_P is the physical solution of the CR as discussed in Sec. IV. An experimentally convenient variable for displaying the data in conjunction with Eq. (5.4) is the circulating power P_{circ} in the resonator, given by

$$P_{\mathrm{circ}} = I^2 Z_0, \quad (5.5)$$

where Z_0 is the characteristic impedance of the stripline resonator used in the experiments. The IMD and circulating power are usually reported in the dimensionless dBm units defined as

$$P(\mathrm{dBm}) = 10\log_{10}\left(\frac{P}{1\ \mathrm{mW}}\right). \quad (5.6)$$

In terms of the modified power variable (5.6), the expressions for the IMD and circulating powers Eqs. (5.4) and (5.5) take the form

$$y = P_{\mathrm{IMD}}(\mathrm{dBm}) = 10\log_{10}\left(\frac{P_{\mathrm{IMD}}}{1\ \mathrm{mW}}\right)$$
$$= 10\log_{10}\left\{\left(\frac{I}{I_{\mathrm{REF}}}\right)^2 S_P^2[\varepsilon(I,T)]\right\} + C(T),$$

$$x = P_{\mathrm{circ}}(\mathrm{dBm}) = 10\log_{10}\left(\frac{P_{\mathrm{circ}}}{1\ \mathrm{mW}}\right) = 10\log_{10}\left[\left(\frac{I}{I_{\mathrm{REF}}}\right)^2\right]. \tag{5.7}$$

The reference current I_{REF} in Eq. (5.7) is that current which generates 1 mW circulating power in the resonator. Expressions (5.7) show that the current dependence of the CR in Eq. (2.16) can be tested against experiment for a fixed temperature by considering the slope of $P_{\mathrm{IMD}}(\mathrm{dBm})$ against $P_{\mathrm{circ}}(\mathrm{dBm})$. According to Eqs. (5.7) and (4.8), the slope of the log-log plot is given by

$$D(x) = \frac{dy}{dx} = 1 + 10\frac{d}{dx}\log_{10}\{S_P^2[\eta(T)10^{x/10}]\}, \tag{5.8}$$

where

$$\eta(T) = \frac{108p(T)\pi^2\lambda_0^4(T)I_{\mathrm{REF}}^2}{(dc)^2}. \tag{5.9}$$

In the low-power limit, $\varepsilon \ll 1$, and from Eqs. (4.4) and (4.10), it follows $S_P^2 \propto \varepsilon^2 \propto I^4 \propto P_{\mathrm{circ}}^2$, which yields a slope $D(x)=3$. In this limit the λ_{NL} has a quadratic current dependence. On the other hand, in the high-power limit, the works of Yip and Sauls[1] and Dahm and Scalapino[6] predict for λ_{NL} a current dependence as $|I|$, which corresponds to a slope of 2, and the transition of slopes between these two power regimes is monotonic. In this work, on the other hand, the slope in the high-power regime is predicted to be 5/3 [Eqs. (4.12) and (5.8)] and the slope transition between these two power regimes is expressed in (5.8). These distinct predictions are amenable for comparison with the data[2] for validation.

Another test of the present theory is to consider a data cut where the circulating power is held fixed in the low-power regime, while the temperature is varied. Since $P_{\mathrm{IMD}} \propto \lambda_{\mathrm{NL}}^2$, we focus on the temperature-dependent factors in λ_{NL}, Eq. (4.2). In addition to such well-known temperature-dependent factors as $\lambda_0(T)$, $P_{\mathrm{IMD}}(T)$ at a constant low power provides a test of the angular integral in (2.17). Its analytical expression is given in Appendix D. Considering the standard temperature dependencies $\Delta_0(T)=\Delta_0\sqrt{1-t^2}$ and $\lambda_0(T)=\lambda_0(T=0)/\sqrt{1-t^2}$, where $t=T/T_C$,[19] and Eqs. (D.2) and (D.3), it follows that

$$\lim_{T\to 0}\lambda_{\mathrm{NL}}(I;T) \propto \frac{I^2}{T}, \quad \lim_{T\to 0} P_{\mathrm{IMD}} \propto \frac{1}{T^2} \quad \text{for} \quad \varepsilon(I,T) \ll 1, \tag{5.10}$$

since for $t<0.1$, both $\Delta_0(T)$ and $\lambda_0(T)$ do not influence the T^{-2} behavior. The same low-temperature divergence was predicted by Dahm and Scalapino.[6]

The third and last prediction to be considered pertains to a direct measurement of λ_{NL} by measuring the stripline resonance frequency as a function of the circulating current. As pointed out above, this method is reliable for sufficiently large frequency shifts. For the case of a quadratic total-current dependence, $f=f_0+f_2I^2$

$$\lambda_{\mathrm{NL}} = \lambda_2\left(\frac{I}{A}\right)^2, \tag{5.11}$$

where A denotes the strip cross section's area, and λ_2 is simply related to the experimentally measured f_2, Appendix E, by

$$\lambda_2 = \frac{f_2}{f}\frac{A^2\lambda_0\Lambda_0}{\Lambda_K}, \quad \Lambda_K = \frac{\mu_0\lambda_0^2\int dSj^2}{I^2},$$

$$\Lambda_0 = \frac{\mu_0(\int dS\lambda_0^2 j^2 + \int dSH^2)}{I^2}, \tag{5.12}$$

where Λ_0 and Λ_K are the linear total and kinetic strip inductances per unit length, which require numerical calculation.[13] For notational clarity, the temperature dependence embedded in the various factors in Eq. (5.12) is suppressed. This experimentally extracted λ_2 is compared below to the theoretically calculated λ_{NL} in the low-power regime (Sec. IV) in order to remain consistent with the quadratic total-current dependence assumed in (5.10).

The theoretical predictions are now compared to recent IMD data.[2,11] The input parameters are the resonator's characteristic impedance $Z_0=33\ \Omega$, the reference current corresponding to a 1 MW circulating power $I_{\mathrm{REF}}=5.5\times10^{-3}$ A, the strip width and thickness $w=150\ \mu$m and $d=0.35\ \mu$m, the gap function [Eq. (A.3)] $\Delta_0(T=0)=0.024$ eV,[18] and the linear penetration depth $\lambda_0(T=0)=0.2\ \mu$m.[2] The $YBa_2Cu_3O_{7-\delta}$ sample measured has an estimated carrier density of 0.34 holes/unit cell. Given the unit cell volume $(a_a)^2a_c$, where $a_a=a_b=0.38$ nm, $a_c=1.17$ nm, the hole density is $n=1.7\times10^{21}\ \mathrm{cm}^{-3}$. The empirical effective mass, identified with the *ab*-plane effective mass, can be extracted either from measured bulk plasma frequency $(\hbar\omega_P)^2=4\pi e^2n(\hbar c)^2/(m^*c^2)$ or from the penetration-depth expression $\lambda^2=m^*c^2/(4\pi e^2n)$.[21] However, the mass values using these two expressions and the carrier density estimated above are not the same. As a compromise we adopt the value $m^*/m_0=2$, which yields $\lambda_0(T=0)\simeq182$ nm and $\hbar\omega_P\simeq1.1$ eV, reasonably consistent with the experimental numbers $\lambda_0(T=0)=200$ nm and $\hbar\omega_P\simeq1.4$ eV.[21] The ensuing Fermi energy is $\mu\simeq0.3$ eV and the c axis Fermi momentum is taken as $k_F(\hat{c})=\pi/a_c=3.2\ \mathrm{nm}^{-1}$.

Figure 6 compares the slope prediction Eq. (5.8) to the experimental IMD-power data at $T=1.75$ K.[2] This particular temperature is chosen to demonstrate most clearly the slope variation with the circulating power. The solid line through the data points is a sixth-order polynomial fit to obtain a smooth differentiable curve for the measured slope. The dashed line is the corresponding derivative. The measured data shows that the slope is nonmonotonic. The calculated slope shows similar behavior except for the discontinuity point where the CR physical solution is abruptly changing. Thus the experimental nonmonotonic slope is interpreted here to indicate the existence of two distinct power-level regimes as predicted in Sec. IV.

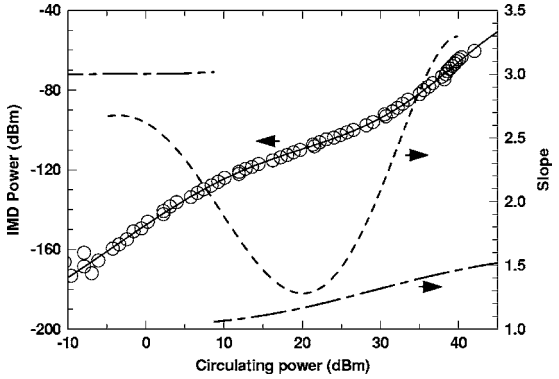

FIG. 6. Comparison of experimental and calculated IMD power slope, Eq. (5.8) at $T=1.75$ K, as a function of the circulating power in dimensionless dBm units, Eq. (5.6). The experimental IMD power and slope (Refs. 2 and 11) are denoted by the open circles and dotted line, respectively, referring to the left and right ordinates. The dash-dot line represents the calculation with the parameters discussed in Sec. V. The discontinuity in the calculated curve mimics the experimental nonmonotonic behavior of the experimental curve at the correct circulating power range.

Figure 7 shows IMD data in the low-power ($\varepsilon \ll 1$), low-temperature regime in relative units, for comparison with the predicted divergence of Eq. (5.10). The predicted T^{-2} low-temperature divergence is clearly manifested. Note also that the calculated curve tracks the experimental curve quite well for almost the entire temperature range. This comparison provides further support for the present theory and the assumed d-wave order-parameter symmetry in YBCO. Data at higher power levels, outside the low-power regime (not shown here), do not show this clean T^{-2} divergence as expected.[2]

Figure 8 plots the values of λ_2 in absolute units vs reduced temperature extracted from the IMD measurements at

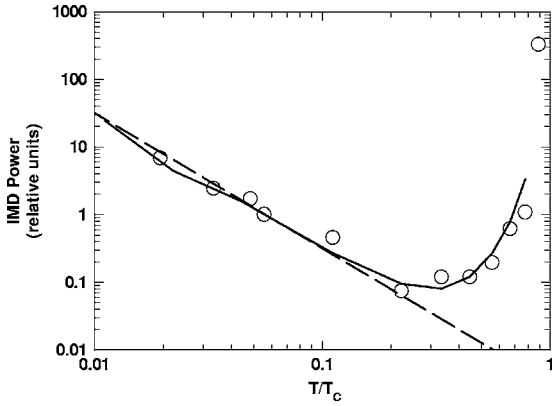

FIG. 7. The measured and calculated IMD power temperature dependence for the low-power regime in relative units, see text. The data, denoted by open circles, are taken from Ref. 2. The calculated curve employs Eq. (5.4) for the IMD power where the variable p is calculated from Eqs. (4.2) and (2.17) and the vector-potential factor $|\vec{A}(q=0)|^2$ is identified with the solution $S_{(1)}$ of Eq. (4.6) for the reasons elaborated in Sec. IV. The parameters are given in Sec. V. The predicted low-temperature divergence, Eq. (5.10), is manifested by the dashed straight line. The solid line is the calculation over an extended temperature range.

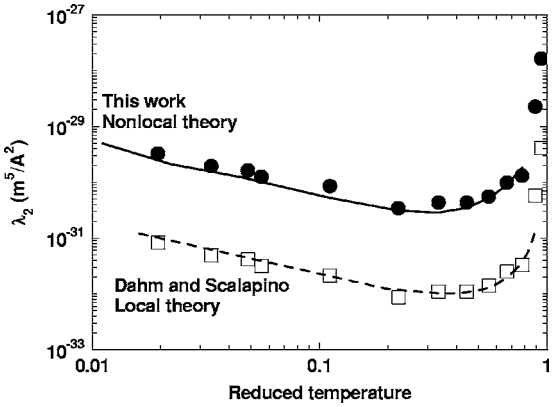

FIG. 8. The temperature dependence of λ_{NL} extracted form resonance-frequency shift data according to nonlocal theory of this work and the local theory approach (Ref. 6) for a low power point; see Sec. V. The chosen power-level point is $P_{circ}=5$ dBm. The nonlocal theory, Eqs. (5.11) and (E.5), employs no free parameters. The local theory, Eqs. (5.11) and (E.7), employs one free parameter j_C, representing the depairing current. The best fit to the data is obtained for $j_C=5.2\times10^8$ A/cm^2.

a low circulating power of 5 dBm. This is the same data as that shown in Fig. 7 but with the absolute value fixed as described in the following. The determination of the absolute λ_2 values begins with extracting the relative values of λ_2 from the measured P_{IMD} since, as Eqs. (5.3) and (5.4) indicate, $\lambda_2 \propto \sqrt{P_{IMD}}$. This process is detailed in Ref. 2. From the IMD measurements directly, one can only obtain relative values of λ_2 because an experimentally verified expression relating IMD power to λ_2 does not exist. The process of obtaining the relative values leaves one free parameter to determine the absolute value of λ_2, which we obtain from measurements of the shift in resonance frequency of the stripline resonator by determining the parameter f_2, as discussed in Appendix E. Because the frequency-shift measurements have lower sensitivity than the IMD measurements, the f_2 must be determined at medium to high power levels. Although we wish to fix the absolute value of λ_2 at low power, the f_2 determined at high power is valid at low power as well, provided the IMD vs power curve has a single slope of 2 throughout the entire range of powers, indicating a simple quadratic dependence of λ_{NL} on current. The data in Ref. 2 show that at 50 K the IMD slope is 2 throughout, and thus, f_2 determined at any power level is valid throughout the whole range. Thus we have used the 50 K data to fix the absolute value of λ_2 shown in Fig. 8.

VI. DISCUSSION AND SUMMARY

In view of the encouraging comparisons between data and these calculations, it is instructive to compare this work with that of Dahm and Scalapino.[6] An important difference is the focus in our calculation on the momentum-space constitutive relation relating the current density and the vector potential. Our approach is a natural extension of the London theory and the classic Meissner effect to the lowest nonlinear order, Eq. (1.1). This extension is derived in the framework of the

general Green-function approach to superconductivity (Gorkov equations).[9] Since all entries in this approach can be extracted from measurable quantities, the resulting expressions entail *no* free parameter. By contrast, the starting point of the Dahm and Scalapino work is the assumed local form of the quasiparticle distribution function in the presence of a current. This approach entails *one* free parameter and, to our knowledge, has been validated only in the limit of a vanishing current.[22] It is therefore to be expected that while the results of this and the Dahm and Scalapino theory share similarities, in particular in the low-power-level regime, they are distinct in content, specifically the nonlocality of the nonlinear terms of the CR emerges from our theory while the Dahm and Scalapino theory is local. As discussed in Sec. III, this nonlocality implies that the nonlinear penetration depth and IMD depend on the total current carried by the strip, e.g., Eqs. (5.11) and (5.12). This property implies in particular that strip edges have no prominent role and Eq. (5.1) is used to extract λ_{NL} from experiments. On the other hand, in the Dahm and Scalapino approach,[6] only the local current density is involved and the current density peaks at the strip edges play an important role; see Eqs. (E.6) and (E.7).

The methodologies of extracting the nonlinear penetration depth from experiment according to the present nonlocal theory and the Dahm and Scalapino local theory are different. According to the latter, to compare the extracted λ_2 with the corresponding theoretical expression Eq. (E.7),[6] the one free parameter of the theory, the depairing current density, is adjusted to $j_C = 5.2 \times 10^8$ A/cm^2; see Fig. 8. According to the present local theory, the extracted λ_2 is given by Eq. (5.12). While these two sets of extracted λ_2 have the same temperature dependence and good fit with the respective theories, they differ substantially in magnitude; see Fig. 8. Another comparison between the present theory and the Dahm and Scalapino results is the slope of the IMD power curve. As Fig. 6 shows for $T = 1.75$ K, the data yield a nonmonotonic slope s, starting at $s=3$ in the low-power regime, dipping down at higher powers to $s \sim 1.5$ before rising again to a value $s \sim 3$. In the local theory, the slope varies from $s=3$ to value $s=2$ monotonically.[6] On the other hand, our theory shares with the Dahm and Scalapino theory the prediction of the low temperature T^{-2} divergence at a fixed low power (Fig. 7) and the prediction of two power-level regimes at low temperatures. It is up to the totality of the data and further theoretical development to resolve which of the two approaches, the local[1,6] or the present nonlocal approach, is the appropriate one.

In summary, a systematic microscopic approach for calculating nonlinear corrections to the Meissner effect, and hence to IMD products, has been presented. It is a natural extension of the linear constitutive relation underlying the London theory. Its predictions compare favorably, both qualitatively and quantitatively, with recent measurements of the power and temperature dependence of IMD in high-quality YBCO films, Figs. 6–8. A distinct advantage of the present approach is that all input parameters are obtainable from measured quantities. The remaining differences between the data and present predictions, e.g., Fig. 6, indicate the need for further extensions of the theory. Efforts in this direction are underway. Finally the present approach is compared to previous work addressing the nonlinear Meissner effect,[1,6] pointing out the similarities and differences between the two approaches. In particular, this approach implies the importance of recognizing the underlying nonlocality of the nonlinear term in the CR while the alternative approach invokes the local current density.[1,6]

ACKNOWLEDGMENTS

This work was supported by the Air Force Office of Scientific Research. D. A. also acknowledges support by the NSWC-Carderock Division ILIR program.

APPENDIX A: THE UNIFORM SUPERCONDUCTOR GREEN FUNCTIONS, *d*-WAVE SYMMETRY GAP FUNCTION, AND ONE-DIMENSIONAL FOURIER TRANSFORMS

For the sake of self-containment and reproducibility of the results in Sec. II, we quote here some useful expressions, all in the cgs unit system. For a uniform superconductor free of an external electromagnetic field, the displacement invariant Green function matrix Eq. (2.4) is given by

$$\hat{G}_0 = \begin{pmatrix} g_0(x,x') & f_0(x,x') \\ f_0(x,x') & -g_0(x',x) \end{pmatrix} = \begin{pmatrix} g_0(x-x') & f_0(x-x') \\ f_0(x-x') & -g_0(x'-x) \end{pmatrix}, \tag{A.1}$$

where the explicit expressions are[9]

$$\{g_0(x-x'), f_0(x-x')\} = [(2\pi)^3 \beta\hbar]^{-1} \sum_{n=-\infty}^{\infty} e^{-i\omega_n(\tau-\tau')} \times \int d\vec{k} e^{i\vec{k}\cdot(\vec{x}-\vec{x}')} \{g_0(\vec{k},\omega_n), f_0(\vec{k},\omega_n)\},$$

$$g_0(\vec{k},\omega_n) = \frac{-\hbar(i\hbar\omega_n + \xi_{\vec{k}})}{(\hbar\omega_n)^2 + \xi_{\vec{k}}^2 + |\Delta(\vec{k})|^2} = g_0^*(-\vec{k},-\omega_n), \quad f_0(\vec{k},\omega_n) = \frac{\hbar\Delta(\vec{k})}{(\hbar\omega_n)^2 + \xi_{\vec{k}}^2 + |\Delta(\vec{k})|^2},$$

$$\omega_n = \frac{(2n+1)\pi}{\beta\hbar}, \quad \xi_{\vec{k}} = e(\vec{k}) - \mu. \tag{A.2}$$

In (A.2), $e(\vec{k})$ denotes the single electron energy in the first Brillouin zone and ω_n are the Matsubara frequencies for fermions where the index n runs over all integers. It can be readily verified that Eq. (A.2) solves Eq. (2.1) for $\vec{A}=0$. In the case of a $d_{x^2-y^2}$ gap symmetry, the gap function can be parametrized as[6,18]

$$\Delta(\vec{k};T) = \Delta(\theta;T) = \Delta_0(T)\cos(2\theta) \tag{A.3}$$

The parametrization in Eq. (A.3) implies a particular orientation of the gap's nodal lines with respect to the direction of current flow; see Fig. 1. It has been shown elsewhere[6] that

results depend rather weakly on the particular orientation; hence hereafter only the nodal-lines orientation implied by Eq. (A.3) is considered. Complementing (A.2) are the orthogonality relations[9]

$$\delta(\vec{x}) = \frac{1}{(2\pi)^3}\int_{-\infty}^{\infty} d\vec{k} e^{i\vec{k}\cdot\vec{x}}, \quad \int_0^{\beta\hbar} d\tau e^{-i(\omega_n-\omega_{n'})\tau} = \beta\hbar\delta_{n,n'}. \tag{A.4}$$

It is implicitly assumed in (A.2) that the gap function is self-consistent to zero order in the vector potential. This self-consistency holds also to first order in $\vec{A}$ by virtue of a symmetry argument:[9] since $\Delta(\vec{r})$ is a scalar, its $\vec{A}$ dependence is expressed with only scalar constructs of $\vec{A}$. The only one such scalar construct linear in the vector potential is $\vec{\nabla}\cdot\vec{A}$, which vanishes by virtue of the gauge choice. Furthermore, the second and all even-order $\vec{A}$-dependent corrections vanish by virtue of a time-reversal symmetry argument; namely, if the gap function contains such terms, so will the ensuing current-density expression, Eq. (2.5), which is inconsistent with the expected property that the current reverses direction when the field does. Consequently the lowest $\vec{A}$-dependent correction to the gap function is of third order. The neglect in this work of this and higher odd-order corrections to the gap function should be considered as part of the approximation scheme adopted here. Its validity hinges on the comparison with the ensuing results and pertinent data. The favorable comparison with data (see Sec. V) indicates that the neglected terms are indeed negligible.[2]

On the other hand, the vector-potential self-consistency acquires the attenuation functional dependence due to the presence of a superconductor strip, which is key to the establishment of approximation Eqs. (2.14). In this sense the approximation Eq. (2.14) is interpreted as the embodiment of the vector-potential self-consistency requirement.

Finally note the one-dimensional Fourier transform definitions of the vector potential and current density used in this work

$$\vec{A}(\vec{r}) = \frac{1}{2\pi}\int d\vec{q} e^{i\vec{q}\cdot\vec{r}}\vec{A}(\vec{q}),$$

$$\vec{A}(\vec{q}) = [A_x(q_z),0,0]\delta(q_x)\delta(q_y), \quad \vec{q} = (q_z,0,0),$$

$$\vec{j}(z) = \frac{1}{2\pi}\int dq_z e^{iq_z z}\vec{j}(q_z), \quad \vec{j}(q_z) = [j_x(q_z),0,0]. \tag{A.5}$$

APPENDIX B: NONLINEAR KERNEL FOR AN *s*-WAVE SUPERCONDUCTOR

The expression Eq. (2.15) is general and hence applies to an *s*-wave superconductor. Note, however, that the angular integration and the Brillouin zone for an *s*-wave superconductor are different than that of a *d*-wave superconductor (see Appendix C). The *s*-wave case has been derived elsewhere[7] by a different technique. It is important to check (2.17) against that previous result. Only results are quoted here for future reference.

In spherical coordinates and for an arbitrary function F the angular integration in (2.17) yields

$$\int d\vec{k}_1\vec{k}_1[\vec{A}(\vec{q})\cdot\vec{k}_1]^2[\vec{A}(-\vec{q})\cdot\vec{k}_1]F(k_1) = \hat{x}|\vec{A}(q)|^2A(q)\frac{4\pi}{5}\int_0^{\infty} dk_1k_1^6F(k_1). \tag{B.1}$$

For a spherical Brillouin zone and ξ as defined in Eq. (A.2), the momentum integration in (B.1) is approximated by

$$\int_0^{\infty} dk_1k_1^6F(k_1) \approx \frac{4k_Fm^3\mu^2}{\hbar^6}\int_{-\infty}^{\infty} d\xi F(k_1(\xi)) \tag{B.2}$$

Employing Eqs. (A.1), (A.2), and (2.16) yields for an *s*-wave superconductor the third-order nonlinear kernel correction

$$K^{(2)}(T) = \frac{2q_S^4\alpha\mu^2k_F\Delta^2(T)}{5\pi^2mc^2(\hbar c)^2\beta\lambda_0^2(T)}\sum_{n=-\infty}^{\infty}\frac{\Delta^2(T)-(2\hbar\omega_n)^2}{[\Delta^2(T)+(\hbar\omega_n)^2]^{7/2}}. \tag{B.3}$$

Expression (B.3) has a different form than that derived in Ref. 7. However, we checked numerically that both forms are identical. This equality implies that the series in Eq. (B.3) has a closed-form sum, i.e., that given in Ref. 7.

In view of the nonlinear penetration-depth divergence at low temperatures for a *d*-wave gap symmetry superconductor as in Eq. (5.10), it is of particular interest to examine the corresponding $T\to 0$ limit of (B.3). In this limit the summation in Eq. (B.3) can be replaced by an integration, i.e.,

$$\int_0^{\infty} dx\frac{1-(2x)^2}{(1+x^2)^{7/2}} = 0. \tag{B.4}$$

Thus, in the $T\to 0$ limit, the kernel $K^{(2)}(T)$ vanishes for an *s*-wave superconductor, opposite to the divergence encountered for a *d*-wave superconductor.

APPENDIX C: THE $\vec{k}_1$ INTEGRATION IN Eq. (2.15) FOR A *d*-WAVE SUPERCONDUCTOR

For the sake of self-containment of this work, the important approximations and details of the $\vec{k}_1$ integration are given here. In the case of a *d*-wave superconductor with the assumed cylindrical Fermi surface,[15] the cylindrical coordinate system is a natural choice. In that coordinate system and the Cartesian coordinate system of Fig. 1, the $\vec{k}_1$-integration, vectors, and scalar products involved are given by

$$\vec{k}_1 = K(\hat{x}\cos\theta + \hat{y}\sin\theta) + \hat{z}k_z, \quad \int d\vec{k} = \int_0^{\infty} dKK\int_0^{2\pi} d\theta\int_{-\infty}^{\infty} dk_z, \quad [\vec{A}(q)\cdot\vec{k}] = A(q)K\cos\theta. \tag{C.1}$$

The *K*-momentum integration in Eq. (C.1) is replaced by

integration over the relative energy $\xi(K,k_z)$, Eq. (A.2). Thus, for the assumed cylindrical Brillouin zone we approximate

$$\xi(K,k_z)=\frac{\hbar^2K^2}{2m_{ab}}+\frac{\hbar^2k_z{}^2}{2m_z}-\mu\approx\frac{\hbar^2K^2}{2m_{ab}}-\mu=\xi(K), \tag{C.2}$$

since $m_z\gg m_{ab}$ for YBCO. Most of the contribution to the integral in Eq. (2.15) comes from the vicinity of the Fermi surface[9]; the contributions from the rest of the integration range are cut off by the Green functions factors in the integrand. It follows therefore that given the approximation Eq. (C.2), the k_z integration in Eq. (2.15) runs over the height of the cylindrical Fermi surface, while the ξ integration, Eq. (C.2), can be extended to infinity. Combining these steps yields

$$\int_{-\infty}^{\infty}dk_z\int_0^{\infty}dKK^5\mathfrak{I}(K,k_z,\theta)\approx 8k_F(\hat{c})\times\left(\frac{m_{ab}}{\hbar^2}\right)^3\mu^2\int_{-\infty}^{\infty}d\xi\mathfrak{I}(K(\xi),\theta), \tag{C.3}$$

where $\mathfrak{I}$ denotes the integrand in (2.15).

The angular integration in Eq. (2.15) is a bit more complex. For the gap function of Eq. (A.3), inserting Eqs. (C.1)–(C.3) into Eq. (2.15), noting the particular angular dependence of the homogeneous Green function factors (Appendix A) by virtue of the gap-function angular dependence, and given that

$$\int_0^{2\pi}d\theta(\cos\theta)^3[\cos(2\theta)]^n=\int_0^{2\pi}d\theta(\cos\theta)^3\sin(\theta)[\cos(2\theta)]^n=0, \tag{C.4}$$

it follows that the angular integration eliminates all but the $\hat{x}$ component in Eq. (2.15), as expected. As for the ξ integration of the $\hat{x}$ component momentum, lengthy algebra yields the simple result

$$\int d\xi\{[\hat{G}_0(\xi,\omega_n)]^4\}_{(1,1)}=\frac{\pi\hbar^4\Delta^2(\theta;T)[\Delta^2(\theta;T)-4(\hbar\omega_n)^2]}{2[\Delta^2(\theta;T)+(\hbar\omega_n)^2]^{7/2}}. \tag{C.5}$$

This result is identical to that embedded in Eq. (B.3) except for the gap-function angular dependence in Eq. (C.5). The latter is taken up in Appendix D.

APPENDIX D: THE ANGULAR INTEGRATION IN Eq. (2.17)

In terms of elliptic integrals according to the definitions in Ref. 24, it can be shown that the angular integration has the closed form

$$\int_0^{2\pi}dx\cos^4(x)\cos^2(2x)\left\{\frac{[\cos^2(2x)-(2B)^2]}{[\cos^2(2x)+(B)^2]^{7/2}}\right\}=\frac{1}{3B^2(1+B^2)^{5/2}}\left[(-1-14B^2+3B^4)E\left(\frac{1}{1+B^2}\right)+B^2(5-3B^2)K\left(\frac{1}{1+B^2}\right)\right]. \tag{D.1}$$

In (D.1) the functions $K(m)$ and $E(m)$ denote the complete elliptic functions of the first and second kind, respectively. Note also the useful relations[20]

$$E(1)=1,\quad \lim_{x\to 0}\left[xK\left(\frac{1}{1+x^2}\right)\right]=0,\quad \sum_{n=-\infty}^{\infty}\frac{1}{(2n+1)^2}=\frac{\pi^2}{4}. \tag{D.2}$$

Comparing the structure of the left-hand side of Eq. (D.1) to Eq. (2.17), it follows that the dimensionless entries to Eq. (D.1) are

$$B(T)=\frac{(2n+1)\pi}{\delta(T)},\quad \delta(T)=\beta\Delta_0(T),\quad \beta=\frac{1}{k_BT}. \tag{D.3}$$

APPENDIX E: EXTRACTING THE ABSOLUTE VALUE OF λ_{NL} FROM THE MEASURED RESONANCE-FREQUENCY SHIFT

The measured change of resonance frequency Δf as a function of the circulating current is related to the nonlinear penetration depth λ_{NL}. Considering the parallel *R-L-C* equivalent circuit of the resonator[25] for which the resonance angular frequency is $\omega=1/\sqrt{LC}$. Consequently,

$$\frac{\Delta f}{f}=-\frac{\Delta L}{2L}, \tag{E.1}$$

where $\omega=2\pi f$, the resonance-frequency shift is $\Delta f\approx df$ and the inductance variation (as a function of the current) is $\Delta L\approx dL$. The value of L is related to the inductance per unit length of the strip Λ as $L=(2/\pi^2)\ell\Lambda$, where ℓ is the strip length. In terms of the MKS units employed hereafter in this appendix, the coordinate system of Fig. 1 and the current and field distributions in and around the strip, Λ is given by[13]

$$\Lambda=\frac{\mu_0\int dydz\lambda^2j(y,z)^2}{I^2}+\frac{\mu_0\int dydzH(y,z)^2}{I^2}, \tag{E.2}$$

where $j(y,z)$ is the current density and $H(y,z)$ is the magnetic field.

1. Nonlocal case

Consider the nonlinear regime of a quadratic dependence on total current,

$$L=L_0+L_2I^2,\quad \Lambda=\Lambda_0+\Lambda_2I^2,\quad f=f_0+f_2I^2, \tag{E.3}$$

$$\lambda = \lambda_0 + \lambda_2 \langle j \rangle^2 = \lambda_0 + \lambda_2 (I/A)^2,$$

where A is the strip cross-sectional area and $\langle j \rangle = I/A$ is the averaged current density. This dependence agrees with empirical observation and the results of discussion in Sec. III. It is implicit in Eq. (E.3) that the nonlocality of the nonlinear contributions is manifest in the expression for λ, which depends on I/A, the average current density, rather than the local current density $j(y,z)$. Equation (E.6) considers the local nonlinearity case.

To a very good approximation, the nonlinear inductance arises primarily from the kinetic term in Eq. (E.2),[6] and the total inductance is to a very good approximation the linear inductance L_0. Thus, inserting (E.3) into (E.2) and (E.1) yields

$$-\frac{2f_2 L_0}{f} \approx -\frac{2f_2 L}{f} = L_2 = \frac{2\ell}{\pi^2} \frac{2\mu_0 \lambda_0 \lambda_2 \int dydz j^2(y,z)}{(AI)^2}. \tag{E.4}$$

Simple manipulations yield

$$\lambda_2 = \frac{f_2}{f} \frac{A^2 I^2 \Lambda_0}{\mu_0 \lambda_0 \int dydz j^2(y,z)} = \frac{f_2}{f} \frac{A^2 \lambda_0 \Lambda_0}{\Lambda_K}, \tag{E.5}$$

where Λ_K the kinetic inductance is given by

$$\Lambda_K = \frac{\mu_0 \lambda_0^2 \int dydz j^2(y,z)}{I^2}.$$

Equation (E.5) relates the λ_2 to the experimentally measured quantity f_2 and to Λ_0 and Λ_K, which has been calculated numerically and verified experimentally.[13]

2. Local case

We turn now to the corresponding derivation in the local Dahm and Scalapino theory,[6] in which the calculated nonlinear penetration depth depends on the local current density $j(y,z)$. Its coefficient λ_2 is given by

$$\lambda = \lambda_0 + \lambda_2 j^2(y,z), \tag{E.6}$$

where

$$\lambda_2 = \frac{\lambda_0 b_\theta}{2 j_C^2},$$

j_C is an adjustable parameter, nominally the depairing current density,[10] and b_θ stands for an angular integral, similar to that in Eq. (2.17).[6] Using Eqs. (E.1) and (E.2) with the insertion of Eq. (E.6) instead of Eq. (E.3), we obtain the expression for λ_2.

$$\lambda_2 = \frac{f_2}{f} \frac{I^4 \Lambda_0}{\mu_0 \lambda_0 \int dydz j^4(y,z)}. \tag{E.7}$$

Note the difference in normalization between Eqs. (E.5) and (E.7), where in the latter the current-density peaks at the strip edges dominate the integral in the denominator. Thus in extracting λ_2 from the experimental f_2 different values of λ_2 will be obtained depending whether the local [Eq. (E.5)] or nonlical [Eq. (E.7)] model is used.

[1] S. K. Yip and J. A. Saul, Phys. Rev. Lett. **69**, 2264 (1992); D. Xu, S. K. Yip, and J. A. Saul, Phys. Rev. B **51**, 16233 (1995).

[2] D. E. Oates, S. H. Park, D. Agassi, and G. Koren, Supercond. Sci. Technol. **17**, S290–S294 (2004) and references therein.

[3] J. H. Claasen, J. C. Booth, J. A. Beall, L. R. Vale, D. A. Rudman, and R. H. Ono, Supercond. Sci. Technol. **12**, 714 (1999); J. C. Booth, L. R. Vale, R. H. Ono, and J. H. Claasen, Supercond. Sci. Technol. **12**, 711 (1999); H. Claasen, J. C. Booth, J. A. Beall, D. A. Rudman, L. R. Vale, and R. H. Ono, Appl. Phys. Lett. **74**, 4023 (1999); J. C. Booth, J. A. Beall, D. A. Rudman, L. R. Vale, and R. H. Ono, J. Appl. Phys. **86**, 1020 (1999).

[4] M. Coffey and J. R. Clem, Phys. Rev. B **48**, 342 (1993); M. Benkraouda and J. R. Clem, Phys. Rev. B **53**, 5716 (1996); J. McDonald, J. R. Clem, and D. E. Oates, Phys. Rev. B **55**, 11823 (1997).

[5] Y. M. Habib, C. J. Lehner, D. E. Oates, L. R. Vale, R. H. Ono, G. Dresselhaus, and M. S. Dresselhaus, Phys. Rev. B **57**, 13833 (1998) and references therein.

[6] T. Dahm, D. J. Scalapino, and B. A. Willemsen, J. Supercond. **12**, 339 (1999); T. Dahm and D. J. Scalapino, Phys. Rev. B **60**, 13125 (1999); T. Dahm and D. J. Scalapino, Appl. Phys. Lett. **81**, 2002 (1997).

[7] D. Agassi and D. E. Oates, J. Supercond. **16**, 905 (2003).

[8] P. G. De Gennes, *Superconductivity of Metals and Alloys* (Benjamin, New York, 1966).

[9] A. Abrikosov, L. Gorkov, and I. Dzyaloshinski, *Methods of Quantum Field Theory in Statistical Physics* (Dover Publications, New York, 1963), section 39; A. L. Fetter and J. D. Walecka, *Quantum Theory of Many Particle Systems* (McGraw-Hill, New York, 1971); M. E. Flatte and J. M. Byers, in *Solid State Physics*, edited by H. Ehrenreich and F. Spaepen (Academic Press, San Diego, 1999), Vol. 52, p. 138.

[10] M. Tinkham, *Introduction to Superconductivity*, 2nd ed. (McGraw-Hill, New York, 1996).

[11] D. E. Oates, S. A. Park, and G. Koren, Phys. Rev. Lett. **93**, 197001 (2004); D. E. Oates, S.-H. Park, D. Agassi, G. Koren, and K. Irgmaier, IEEE Trans. Appl. Supercond. **15**, 3589 (2005).

[12] J. D. Jackson, *Classical Electrodynamics*, 2nd ed. (Wiley, New York, 1975), pp. 334–339.

[13] D. M. Sheen, S. M. Ali, D. E. Oates, R. S. Withers, and J. A. Kong, IEEE Trans. Appl. Supercond. **1**, 108 (1991).

[14] M. Tinkham, *Introduction to Superconductivity* (Ref. 10), Appendix 3.

[15] M. I. Salkola, A. V. Balatsky, and D. J. Scalapino, Phys. Rev. Lett. **77**, 1841 (1996); P. J. Hirschfeld, W. O. Putikka, and D. J.

Scalapino, Phys. Rev. B **50**, 10250 (1994).
[16] M. Tinkham, *Introduction to Superconductivity* (Ref. 10), pp. 89–91.
[17] M. Tinkham, *Introduction to Superconductivity* (Ref. 10), pp. 94–96.
[18] For example, in J. Y. T. Wei, N. C. Yeh, D. F. Garrigus, and M. Strasik, Phys. Rev. Lett. **81**, 2542 (1998).
[19] M. Tinkham, *Introduction to Superconductivity* (Ref. 10), p. 381.
[20] G. Arfken, *Mathematical Methods for Physicists*, 3rd ed. (Academic Press, Orlando, 1985), p. 324.
[21] C. P. Poole, A. A. Farach, and R. J. Creswick, *Superconductivity* (Academic Press, San Diego, 1995), p. 502; P. B. Allen, W. E. Pickett, and H. Krakauer, Phys. Rev. B **37**, 7482 (1988); P. B. Allen, W. E. Pickett, and H. Krakauer, Phys. Rev. B **36**, 3962 (1987); R. T. Collins *et al.*, IBM J. Res. Dev. **33**, 238 (1989).
[22] J. Bardeen, Phys. Rev. Lett. **1**, 399 (1958).
[23] T. Van Duzer and C. W. Turner, *Principles of Superconductive Devices and Circuits* (Elsevier, New York, 1981).
[24] S. Wolfram, *The Mathematica Book* (Wolfram Media, Champaign, IL, 1999), p. 774; L. M. Milne-Thomson, in *Handbook of Mathematical Functions*, edited by M. A. Abramowitz and I. A. Stegun, Natl. Bur. Stand. Applied Mathematics Series.55 (GPO, Washington, DC, 1964), p. 590.
[25] D. E. Oates, A. C. Anderson, and P. M. Mankiewich, J. Supercond. **3**, 251 (1990).